Fracture failure analysis of baseplates in a fluidic amplifier made of WC-11Co cemented carbide

H. Liu, K. Yin, J.M. Peng, Q.L. Yin

College of Construction Engineering, Jilin University, Changchun (China)
523772622@qq.com

ABSTRACT. A fluidic amplifier is a crucial automatic control component in a liquid jet hammer used to drill hard formations in the oil industry. This study aims to determine the true causes of the fracture failure of baseplates in a fluidic amplifier made of WC-11Co cemented carbide in a very short period of time. Computational fluid dynamics (CFD), theoretical estimation, and finite element analysis (FEA) were employed to analyze the effect of static and dynamic loads on the strength of the baseplates. Fractographic, metallographic, and processing defect analyses were also carried out. The FEA results showed that the static and dynamic loads caused stress concentrations at the actual fracture locations, and the effect of working loads on material strength was allowable and safe. Fracture surfaces exhibited typical characteristics of a brittle fracture. The metallographic analysis revealed that a specific amount of brittle eta-phase (η-phase) was present in the material. The microstructure of the processing cutting zone was inspected and the results revealed that some voids, pores, and microcracks were formed on the processing surface. The manufacturing and processing defects resulted in low stress fracture failure of the baseplates.

KEYWORDS. Fracture analysis; Fluidic amplifier; WC-Co cemented carbide; Numerical simulation; Microstructure.

INTRODUCTION

I n an oil drilling field, drilling hard formations is an arduous problem that demands prompt solution all the time, especially in deep wells. As deep-oil resource exploration continues to increase, the depths of oil wells have become increasingly deeper and the rocks at such great depths have become harder to drill. The hydraulic hammer was considered as one of the best tools to drill hard formations for many years [1-3]. The application of conventional rotary drilling to drill hard formations have several weaknesses such as high cost, low rate of penetration (ROP), and short service life of drilling tools [4-9]. The liquid jet hammer technique is a highly efficient method that overcomes the disadvantages of conventional drilling methods for hard formations.

The liquid jet hammer is a down-the-hole tool that is used to exert an impacting force on the drill bit [4]. It has been widely applied in exploration core drilling since its invention in the 1970s and was crucial in drilling the No. 1 hole of the Project of China Continental Science Drilling [5-7]. Exploration core drilling efficiency can be improved by more than 30%, higher core recovery rates can be obtained, and straighter holes can be drilled when a liquid jet hammer is used [4, 5]. In oil and gas drilling, a number of field tests have proven that liquid jet hammer could increase drilling efficiency by more than 120% in hard formations [8-10]. As shown in Fig. 1, the YSC178 liquid jet hammer [5, 11] is placed at an oil drilling platform of the Zhongyuan oil field and is connected at the bottom of the drill pipes.
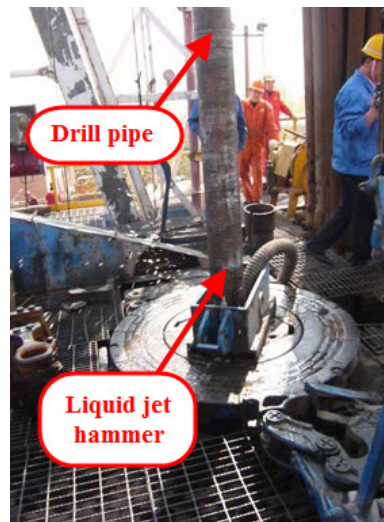
Figure 1: Test platform of a liquid jet hammer at the Zhongyuan oil field.

DESCRIPTION OF THE FLUIDIC AMPLIFIER AND THE LIQUID JET HAMMER

A bistable fluidic amplifier comprises two baseplates, two lid plates, and a splitter. These components are connected to one another by pins and bolts, as shown in Fig. 2. The supply jet fluids that enter the fluidic amplifier have several flow characteristics, such as attachment, switching, and vortex. The supply jet switching mechanism is a feedback loop that is designed between the control nozzle and the output channel on each side, which is relatively similar to the feedback loop in a fluidic oscillator for flow metering or flow separation control [4].
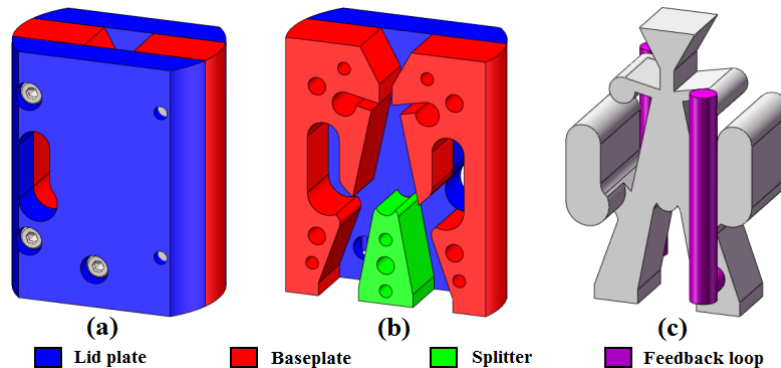
Figure 2: Configuration of the bistable fluidic amplifier in a liquid jet hammer. (a) Whole amplifier; (b) Amplifier removed a lid plate; (c) main fluid domain of an amplifier

The liquid jet hammer has several major parts, namely, fluidic amplifier, cylinder, piston, mass block, and anvil. A bistable fluidic amplifier is employed to regulate the actuator of a liquid jet hammer. The actuator comprises a cylinder, a piston, and a mass block. The piston and the mass block were linked using a cone connection to form an impacting body. The working principle of a liquid jet hammer is shown in Fig. 3. The drilling fluids enter the liquid jet hammer through the supply nozzle on the fluidic amplifier and are turned into high-pressure jet fluids. The jet fluids randomly attach to the left or right sidewall. (1) Downward stroke of the impacting body: The jet fluids attach to the left sidewall and enter the upper chamber of the cylinder through the output channel (e). The high-pressure fluids push the impact body to strike the anvil. The fluids at the lower chamber of the cylinder are extruded into the annular space between the hammer and outer sleeve through the vent (d). When the piston moves to the stopping end of the cylinder, the fluid pressure in the upper chamber of the cylinder increases. This pressure signal propagates along the feedback loop and reaches the control nozzle (a), which signals the jet fluids attached to the left sidewall to switch to the right sidewall. (2) Backward stroke of the impacting body: The jet fluids attach to the right sidewall and enter the lower chamber of the cylinder through the output

channel (f). The high-pressure jet fluids push the impact body to return to its original position. The fluids in the upper chamber of the cylinder are extruded into the annular space between the hammer and outer sleeve through the vent (c). When the piston moves to the stopping end of the cylinder, the fluid pressure in the lower chamber of the cylinder increases. The pressure signal propagates along the feedback loop and reaches the control nozzle (b), which signals the jet fluids attached to the right sidewall to switch to the left sidewall [4,5].

The bistable fluidic amplifier controls the high-pressure drilling fluids to enter alternately in the upper and lower chambers, which causes the reciprocating motion of the impacting body. Impact force is generated periodically and impact energy is transferred to the anvil and tricone roller bit.
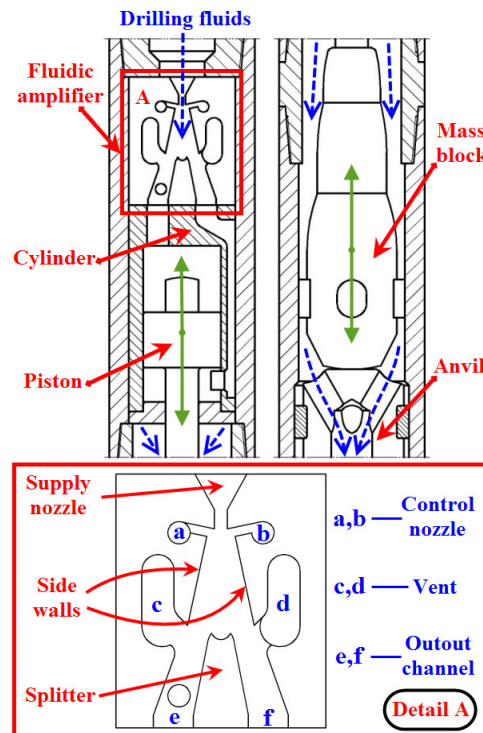
Figure 3: Working principle of a liquid jet hammer and a fluidic amplifier.

DESCRIPTION OF FAILURE SCENARIO

The fluidic amplifier is an automatic control device that uses several fluid properties [12] and is regarded as the most critical part in a liquid jet hammer. Therefore, the service life of a fluidic amplifier has an important effect on the normal work of a liquid jet hammer. The work condition of a fluidic amplifier is extremely complex because of high-velocity drilling fluids that contain abrasive particles. In previous oil-drilling applications, the velocity of the drilling fluids that enter the supply nozzle reaches 60 m/s to 100 m/s, and the failure of a fluidic amplifier is mainly due to abrasive erosion [13,14]. High-velocity solid particles in drilling fluids wear away the inner structures of a fluidic amplifier, and significant erosion pits can be seen on the inner surface of a fluidic amplifier. Abrasive erosion leads to the failure of the fluidic amplifier such that the service time of a fluidic amplifier ranges from a few hours to a dozen hours.

The fluidic amplifier in this study was made of WC-11Co cemented carbide, as shown in Fig.4 (a), with an expected service life of 120 h in complex conditions. However, the accident occurred that the liquid jet hammer only worked within several seconds in the test. The fluidic amplifier from the YSC178 liquid jet hammer was taken out, and three fracture locations were found at the baseplates of the fluidic amplifier, as shown in Fig. 4(b). The appearance of the fractured section was smooth and no evident plastic deformation, such as elongation or bending, were observed. No signs of abrasive erosion were observed on the surface of the sidewalls and the supply nozzle. This form of failure was noticeably different from those in previous tests [13, 14]. This failure was evidently a brittle fracture, but not abrasive erosion.

WC-11Co cemented carbide is a typical brittle composite material; fracture failure exhibits no distinct plastic deformation. The yield strength of this material is not easily determined by experimental tests. A sudden fracture failure may occur in

WC-11Co cemented carbide if the actual local stress exceeds the material strength limit. In addition to different unexpected failure scenarios, the manufactured material and loading situation of the fluidic amplifier in this study are different from those in previous tests.

<center>(a)   (b)</center>
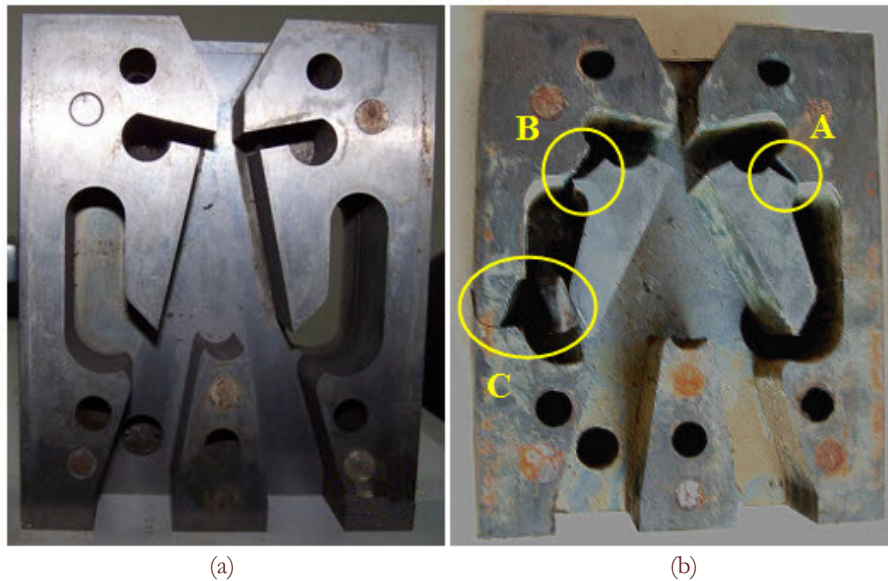
Figure 4: Intact and damaged baseplates of the fluidic amplifier. (a) Intact fluidic amplifier; (b) three fracture locations on the baseplates.

(1) New material. WC-11Co cemented carbide was used to manufacture a fluidic amplifier instead of 35CrMo alloy steel in the previous test to reduce abrasive erosion. This material exhibits several good material properties, such as high hardness, high strength, good wearing resistance, and great corrosion resistance [14].

(2) No disc springs. A set of disc springs used in the previous test was installed at the top of the fluidic amplifier. These disc springs were adjusted to provide a small fitting allowance among the components inside a liquid jet hammer; in this way, sealing problem could be solved and cylinder deformation could be avoided. However, the disc springs with an unreasonable design and unpredictable fitting allowance can lead to more serious leakage and abrasive erosion. Therefore, the disc springs in this test were removed from a liquid jet hammer [13, 14].

In this study, the following failure analyses were comprehensively investigated: (1) strength analysis with numerical simulations; (2) fractographic analysis; (3) metallographic analysis; (4) and processing defect analysis.

NUMERICAL SIMULATIONS FOR STRUCTURE STRENGTH ANALYSIS OF THE FLUIDIC AMPLIFIER

In this study, the simplified physical process explains that before the liquid jet hammer has applied work on the drilling fluid pressure and the axial static pressure caused by threaded connection have generated pre-stress on the fluidic amplifier, the impact force caused by the backward stroke of the impacting body is exerted at the bottom of the fluidic amplifier. The force analysis diagram of the fluidic amplifier is shown in Fig. 5. However, the effect of the static and dynamic loads on the material strength of the fluidic amplifier remains unknown.

The "implicit-explicit sequence solving" analysis method [15] is employed to investigate the reason for fracture failure. The following is the procedure of the numerical analysis: (1) the drilling fluid pressure on the sidewalls of the baseplate and the terminal velocity of the backward stroke of the impacting body can be calculated using the CFD method; (2) the axial static pressure on the fluidic amplifier can be theoretically estimated; (3) the calculated drilling fluid and axial static pressures are set at the boundary conditions in the implicit static calculation analysis, and pre-stress static results could be obtained by an implicit solver; (4) based on the implicit results, the terminal velocity of the backward stroke of the impacting body is set to an initial condition in the explicit solver; (5) the dynamic load results can be obtained using the explicit solver of ANSYS/LS-DYNA. The effect of the static and dynamic loads on the material strength of the fluidic amplifier can be determined by comparing the first-principle and equivalent stresses to the strength limit.
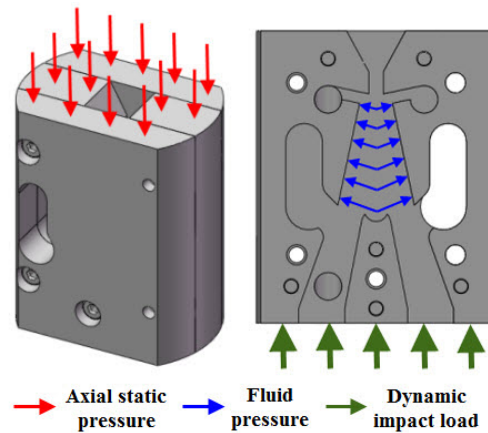
Figure 5: Force analysis diagram of the fluidic amplifier.

DETERMINATION OF BOUNDARY AND INITIAL CONDITIONS USING CFD

Computational domain and mesh model

This study combined the simulation of the fluid and the motion of the impacting body by using the dynamic mesh technique and a user-defined function(UDF) [16-21]. The computational domain of the fluid field in the YSC178 liquid jet hammer includes the fluid field of a fluidic amplifier, two side passages connected to the vents of the fluidic amplifier, the upper and lower chambers of the cylinder, as well as the connecting passages between the fluidic amplifier and the cylinder.

The computational domains were meshed using the Altair Hypermesh software. The mesh model was used as the starting volume mesh for the dynamic mesh modeling technique. The mesh of the computational domains was shown in Fig. 6. In this mesh model, 1636 out of 37713 elements were pentahedron, and the rest were hexahedral.
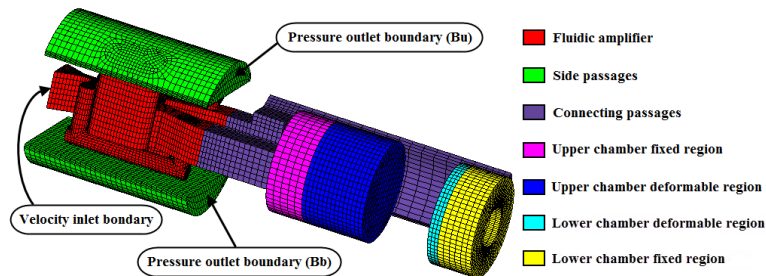
Figure 6: Computational domain and boundary conditions.

The mesh dependence test was performed for the mesh model of the YSC178 liquid jet hammer. Three sets of meshes were tested. As shown in Tab. 1, the maximum difference between the obtained results is less than 5.2%. The coarse mesh can also provide sufficient mesh independency. Considering the computational time cost versus the model accuracy, computations were performed using the medium mesh.

	Number of elements	Fluid pressure [a] (MPa)	Terminal velocity [b] (m/s)
Coarse mesh	18562	0.78	1.90
Medium mesh	37713	0.81	1.85
Fine mesh	75169	0.82	1.82
% Difference [c]		5.13	4.39

[a] The approximate fluid pressure on the sidewalls of the fluidic amplifier.
[b] The terminal velocity of backward stroke of the impacting body.
[c] The percentage difference between the coarse and fine mesh.

Table 1: The details of the mesh dependence test for the YSC178 liquid jet hammer.

Initial and boundary conditions of CFD

The computation had two steps: the steady and unsteady simulations. The result of the steady computation provided the initial conditions for the unsteady simulation.

In the steady simulation step, a velocity inlet boundary condition was set at the supply nozzle inlet of the fluidic amplifier (Fig. 6). At the experimental test, the pump flow rate was 0.02 m³/s, and the velocity inlet boundary condition was set at 71.4 m/s. Two vents and side passages provided two outlets in the computational domain. Two outlet faces, namely, Bb and Bu, were defined as the pressure outlet boundary conditions. Bb and Bu were the outlet faces of the side passage connected to the lower and upper chambers of the cylinder, respectively. At Bb, the pressure outlet boundary condition was set at atmospheric pressure. At Bu, the pressure outlet boundary condition was set at least two times higher than the atmospheric pressure to enforce the main jet attached to the sidewall corresponding to the lower chamber. In this manner, the upward movement of the impacting body was initiated.

In the unsteady simulation step, the velocity inlet boundary condition was the same as that in the static simulation. However, the pressure outlet boundary conditions were set to atmospheric pressure at both Bb and Bu. Thus, the possibility is the same as that of the supply jet attached to either sidewall when the impacting body reached the stopping end of the cylinder.

CFD results

The pressure distribution (Fig. 7) illustrates that the fluid pressure on the sidewalls is about 0.7 MPa when the flow rate in the test was 0.02m³/s. The velocity distribution (Fig. 8) illustrates that the terminal velocity of the backward stroke of the impacting body is about 1.85 m/s.

The fluid pressure on the sidewalls is one of the boundary conditions in the "IMPLICIT ANALYSIS" section. The terminal velocity of the backward stroke of the impacting body is one of the initial conditions in the "EXPLICIT ANALYSIS" section.
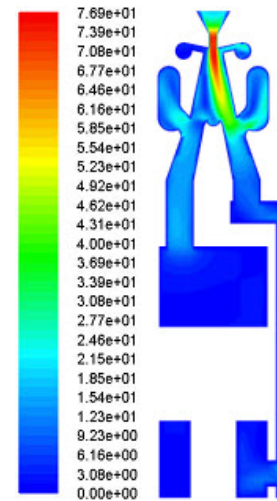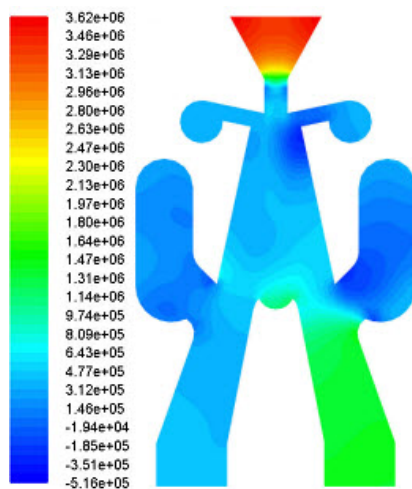
Figure 7: Pressure distribution when the flow rate was 0.02 m³/s.

Figure 8: Velocity distribution when the impacting body reached the stopping end.

ESTIMATION OF THE AXIAL STATIC PRESSURE

The threaded connection between the outer tubes generated the axial static pressure on the fluidic amplifier. Based on the main parameters of API 5 1/2 IF thread (Tab. 2) [22], the axial static pressure of the threaded connection on the fluidic amplifier was estimated by following a series of formulas.

Friction coefficient: $f = 0.1$; Friction angle: $\rho = \arctan f = 5.71°$

Equivalent friction coefficient: $f' = f / \cos\beta = 0.1 / \cos 30° = 0.115$

Equivalent friction angle: $\rho' = \arctan f' = 6.59°$

Thread circumference at the minor diameter: $D_c = (D_L + D_s)/2 - h = (162.48 + 141.31)/2 - 2.831 = 149.064\,mm$

Lead of thread: $L = 1\,inch / n = 25.4\,mm/4 = 6.35\,mm$

Helix angle: $\psi = \arctan L/\pi D_c = \arctan 6.35/\pi \cdot 149.064 = 0.01356$

Max output torsional moment of Kelly spinner: $T = 2200\,N \cdot m$

Axial force:

$$F = \frac{T}{\frac{D_c}{2}\tan(\psi + \rho')} = \frac{2200\,N \cdot m}{\frac{149.064 \times 10^{-3}\,m}{2} \times \tan(0.01356° + 6.59°)} = 254974\,N$$

Top plane dimensions of the fluidic amplifier: $S = 9107\,mm^2$

The axial static pressure on the fluidic amplifier: $P = \dfrac{F}{S} = \dfrac{254974\,N}{9107\,mm^2} \approx 28\,MPa$

In the section of *Implicit analysis*, the axial static pressure at the top of the fluidic amplifier was 28 MPa.

Connection style and size	Thread form	Taper	Half angle	Threads per 25.4 mm	Thread height truncated	Large dia. of pin	Small dia. of pin
		T	β	n	h	D_L	D_S
5 1/2 IF	V-065	1/6	30°	4	2.831	162.48	141.31

(Dimensions in millimeters, unless otherwise specified)

Table 2: The main parameters of API 5 1/2 IF thread.

STRUCTURE STRENGTH ANALYSIS USING FEA

S tructural implicit-to-explicit sequential solutions can be used for a broad range of engineering problems, wherein the initial static stress state of the structure affects its dynamic response in ANSYS LS-DYNA [15,23].

In this implicit-to-explicit sequential solution, a calculated drilling fluid pressure of 0.7 MPa and an axial static pressure 28 MPa are set to be preloads in the ANSYS implicit analysis. The nodes of any element that are only used in the explicit analysis were completely constrained. The information of nodes and elements obtained from the ANSYS implicit solver are written in the ANSYS LS-DYNA dynamic relaxation file. The explicit analysis can be conducted after setting the initial velocity at 1.85 m/s and other calculated conditions. The explicit solver uses the displacement results stored in the relaxation file for the stress initialization of the model. The explicit analysis begins at time zero with a stable preloaded structure. Then the explicit analysis can be solved and completed.

Mesh model	Material	Density (kg/m³)	Elastic modulus (MPa)	Poisson ratio	Element type (Implicit)	Element type (Explicit)	Material model (Implicit)	Material model (Explicit)
Fluidic amplifier	WC-11Co	1.42e+4	6.0e+5	0.22				Bilinear isotropic hardening model
					Solid 185	Solid164	Linear elastic model	
Cylinder	35CrMo	7.76e+3	2.07e+5	0.3				Linear elastic model
Impacting body							Rigid model	Rigid model

Table 3: Material and element properties of the components

Mesh model

The simplified geometry models of the fluidic amplifier, the cylinder, and the impacting body are built. Material and element properties corresponding to each component are shown in Tab. 3. The material attributes of 35CrMo were assigned to the mesh models of the cylinder and the impacting body. The material attributes of WC-11Co were assigned to the mesh model of the fluidic amplifier. In the implicit analysis, the element type and material model of the fluidic amplifier were defined as SOLID 185 and the linear elastic model, respectively. In the explicit analysis, the element type and material model of the fluidic amplifier were defined as SOLID 164 and the bilinear isotropic hardening model, respectively. The material models of the cylinder and the impacting body were defined as the linear elastic model and the rigid body, respectively. The element type of the cylinder and the impacting body was the same as that of the fluidic amplifier.

A short, solid cylinder was used to replace the actual cylinder for simplification, and the thickness of cylinder was defined as the actual value. The mesh model contained the fluidic amplifier, the cylinder and the impacting body. Some weak areas were meshed finely, such as those in control nozzles, sidewalls, and vents. The mesh model is shown in Fig. 9. In this mesh model, 2473 out of 47455 elements were pentahedron, whereas the rest were hexahedral.

The mesh dependence test was performed for the mesh model of FEA. Three sets of meshes were tested. As shown in Tab. 4, the maximum difference between the obtained results is less than 4.5%. The coarse mesh was observed to provide a sufficient mesh independency. Thus, the computations were performed using the medium mesh.
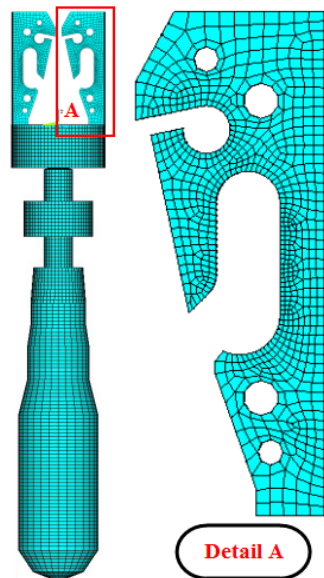
Figure 9: Mesh model of FEA

	Number of elements	Maximum first-principle stress (MPa)	Maximum equivalent stress(MPa)
Coarse mesh	24786	835	732
Medium mesh	47455	842	752
Fine mesh	95622	868	765
% Difference [a]		3.8	4.3

[a] The percentage difference between the coarse and fine mesh.

Table 4: The details of the mesh dependence test for the mesh model of FEA.

Implicit analysis

An axial static pressure of 28 MPa was applied on the top of the fluidic amplifier, whereas a fluid pressure of 0.7 MPa was applied on the sidewalls. After defining the necessary boundary conditions, the implicit analysis can be conducted. The equivalent stress distribution of the implicit analysis is shown in Fig. 10. The equivalent stress concentration of 251 MPa appeared at the location between the control nozzle and the vent. The maximum equivalent stress was too small to cause the fracture failure.

All results that contained the node, element, constraint, and boundary information were written in the relaxation file, which were prepared for the explicit analysis.

-30.929   0.357   31.644   62.926   94.215   125.502   156.787   188.074   219.359   251.645
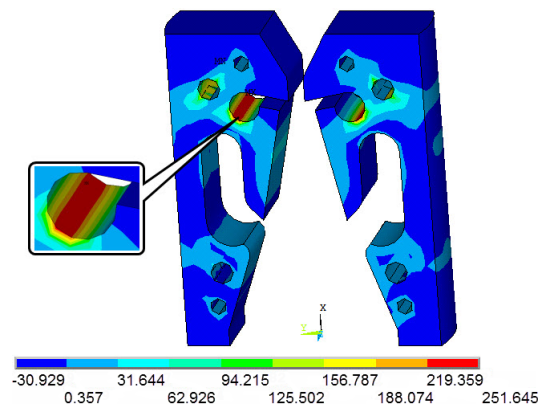
Figure 10: The equivalent stress distribution of the implicit analysis.

Explicit analysis

Boundary conditions, initial conditions, and contact parameters were redefined on the basis of the actual situation after the relaxation file was initialized. A terminal velocity of 1.85 m/s, which was calculated using the CFD method, was applied to define the initial velocity of the impacting body. An impacting body mass of 63 kg was used to define the inertia options.

-80.817   19.519   119.855   220.191   320.527   420.863   521.198   621.535   721.871   822.207

(a) First-principle stress

-56.332   33.947   124.226   214.505   304.784   395.063   485.342   575.621   665.901   756.179

(b) First-principle stress

-83.566   5.086   93.738   182.391   271.042   359.693   448.346   536.998   625.651   714.302

(c) Equivalent stress

-169.604   -74.239   21.126   116.491   211.856   307.221   402.586   497.951   593.316   688.681

(d) Equivalent stress

Figure 11: Typical stress distributions of the explicit analysis. (a) and (b) are first-principle stress distribution; (c) and (d) are equivalent stress distribution.

The typical results of the explicit analysis are shown in Figs. 11(a–d). Figs. 11(a and b) and 11(c and d) show the first-principle and equivalent stress distributions at different times, respectively. In Fig. 11(a), the maximum first-principle

stress of 822 MPa was observed on the upper surfaces of the two vents subjected to tensile stress. The lower surface of the two control nozzles and the outboard walls of the two vents were found on the compressive stress regions. In Fig. 11(b), the maximum first-principle stress of 756 MPa was simultaneously observed at the location of the two control nozzles and the outboard walls of the two vents. In the opposite image of Fig. 11(a), the lower surfaces of the two control nozzles and the outboard walls of the two vents were subjected to tensile stress. In Fig. 11(c), the lower surfaces of the two control nozzles and the upper surfaces of the two vents showed equivalent tensile stress concentration at the same time. The maximum equivalent stress was 714 MPa. In Fig. 11(d), the outboard walls of the two vents were subjected to a wide range of equivalent stress concentration. The stress distributions in Fig. 11 illustrated that tensile and compressive stresses changed alternately at the actual fracture locations on the baseplates. The stress variation and great stress gradient adversely affected material strength.

Although stress variation was complex when the baseplates were subjected to a dynamic impact load, the maximum stress was less than the strength limit of approximately 2100 MPa. In a typical operation of a liquid jet hammer, the fluidic amplifier was in a safe working state. Thus, fracture failure within a very short period of time was impossible to occur in an intact fluidic amplifier under normal working conditions. However, the FEA results revealed that the static and dynamic loads generated stress concentration at the actual facture locations. According to the structure strength analysis by FEA, low strength and abnormal loads can be ruled out as the causes of failure. However, once the material showed minor defects, a low stress brittle fracture can occur within a short period of time. This assumption is consistent with the failure scenario in Fig. 4. Therefore, some tests for the failed material were conducted in the following contents.

EXPERIMENTAL TESTS

Fractographic analysis

Scanning electron microscopy (SEM) was performed to investigate the microstructure of the fracture locations A, B, and C on the baseplates. The smooth fracture morphology and the absence of distinct ductile fracture features, such as ductile dimples, are shown in Figs. 12(a) and 12(c). Many pores were visible. Figs. 12(b–f) show some transgranular and intergranular cleavage fracture surfaces. "River line" marking patterns, fine pores, and secondary cracks are shown in Figs. 12(e) and 12(f). These pores can easily cause the discontinuity among each phase and form the crack origins. These defects produced stress concentration and reduced material strength. All of the fracture characteristics were typical brittle fractographic observations. The bright edges and surfaces in Fig. 12 were the carbon-deficient features, in which the carbon-deficient phase can increase material brittleness. Therefore, the microstructure of the three fracture locations of the baseplates exhibited a typical brittle fracture.
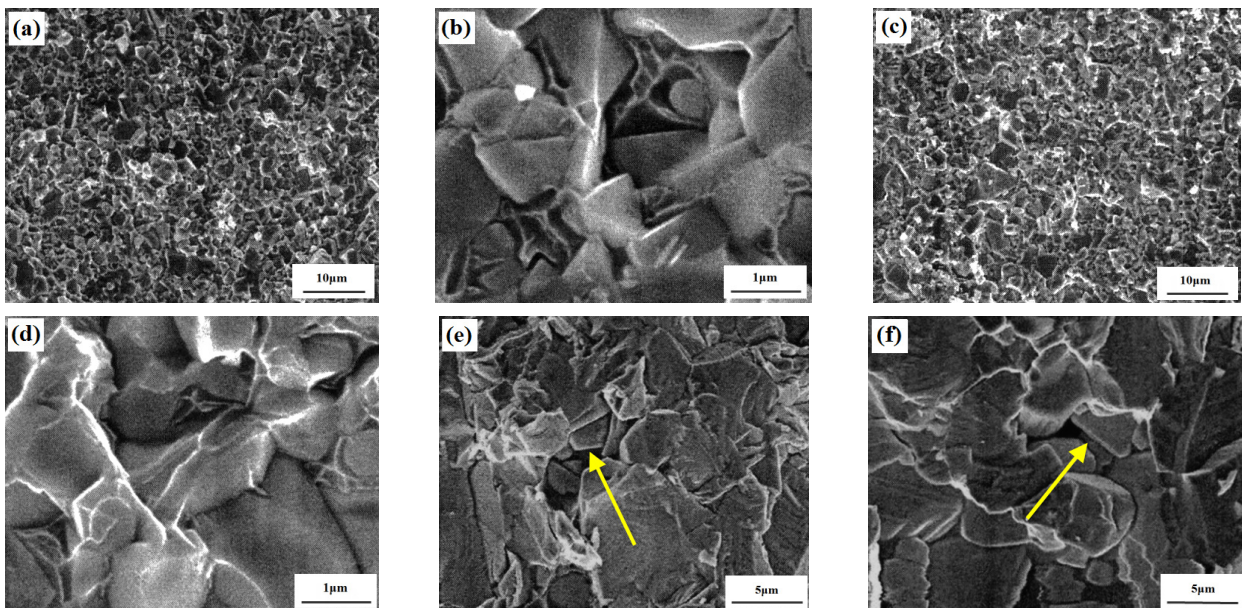
Figure 12: SEM micrographs of the fracture locations A, B, C on the baseplates in Fig.4(b). (a) and (c) are the fractographs of location A and B, respectively; (b) and (d) are magnified figures of (a) and (c), respectively; (e) and (f) are the fractographs of location C.

Metallographic analysis

Three metallographic sections, which were respectively perpendicular to the fracture surfaces A, B, and C in Fig. 4, were prepared for the observation. After a color developing agent was applied, some non-uniform distributed eta-phases appeared on the polished surfaces (Fig. 13). The dark regions in the metallographs were the eta-phase regions. Eta-phase (η-phase) is a complex carbide compound of W and Co. η-phase has a formula of $W_x Co_y C_z$. Eta phase is also a carbon-deficient form of the cemented carbide with hard and brittle performance. This material is generally considered harmful to the material performance of cemented carbide. In WC-11Co cemented carbide sintering, lower carbon content generated higher eta-phase content and more pores. These carbon-deficient phases can significantly reduce material strength.

(a)	(b)	(c)
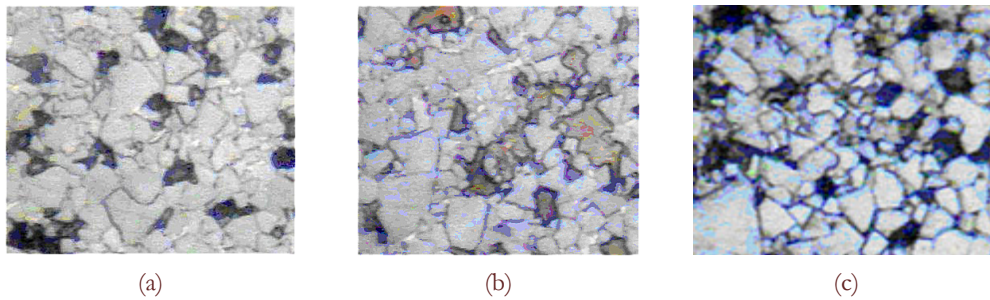
Figure 13: Metallographic sections of the fracture surfaces. (a), (b) and (c) are the metallographs of the fracture surfaces A, B and C in Fig.4, respectively.

Processing defect analysis

Given the complex shapes of the baseplates and high hardness of WC-11Co cemented carbide, conventional machining operations cannot be achieved. The baseplates of a fluidic amplifier were processed by the wire electrical discharge machining (WEDM) cutting method. WEDM is a non-traditional, thermoelectric process, which erodes material from the work piece by a series of discrete sparks between a work electrode and a tool electrode immersed in a liquid dielectric medium. These electrical discharges melt and vaporize minute amounts of the work materials, which are then ejected and flushed by using a dielectric medium [24,25].

However, the microcracks on the cemented carbide easily developed during machining. The crack initiation and voids of the WEDM cutting zones adjacent to the fracture surfaces were detected using SEM (Fig. 14). Many voids, pores, and microcracks were observed by SEM. These defects can reduce material strength and cause total failure. A large thermal gradient between the cutting surface and internal material structure during WEDM can generate microcracks and thermal residual stresses.
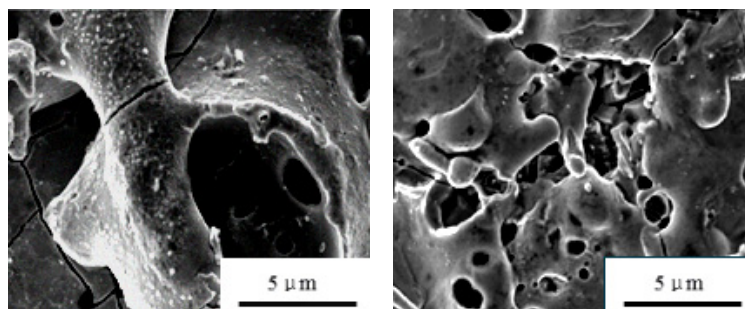
Figure 14: SEM views of cutting zones adjacent to fracture surfaces.

DISCUSSIONS AND CONCLUSIONS

A series of numerical simulations and tests were performed. The main conclusions are summarized as follows:
1. The static and dynamic loads generated stress concentration and great stress variations at the actual fracture locations using CFD and FEA under normal working states of a liquid jet hammer. However, the maximum stresses were less than the material strength limit of WC-11Co cemented carbide. The effect of static and dynamic loads on the material strength of the baseplates was allowable and safe.

2. The SEM microstructures of the fracture surfaces revealed that clear characteristics of a brittle fracture can be observed. Such characteristics were transgranular and intergranular cleavage fracture, pores, secondary cracks, and carbon-deficient phase. The metallographic analysis results revealed that the presence of a specific amount of eta-phase can increase material brittleness. The processing defects of the WEDM cutting method were observed under SEM. Many voids, pores, and microcracks were found on the cutting surfaces at the vicinity of the fracture locations. These defects can reduce material strength and cause total failure.

3. The results of numerical simulations and experimental tests indicated that the baseplate fracture accident was the brittle fracture failure with low stress. Fracture failure was attributed to the manufacturing defects in WC-11Co cemented carbide sintering and the processing defects of the WEDM cutting method.

REFERENCES

[1] Han, G., Bruno, M., Lao, K.H., Percussion drilling in oil industry: review and rock failure modeling, The AADE national technical conference and exhibition, April 5-7, Houston, USA, (2005).

[2] Wanamaker, J.A., Rotary percussion drilling in West Texas, World Oil, (1951) 182-187.

[3] Melamed, Y., Kiselev, A., Gelfgat, M., Dreesen, D., Blacic, J., Hydraulic hammer drilling technology: developments and capabilities, J. Energ. Resour. Technol., 122(1) (2000) 1-8.

[4] Yin, K., Wang, M.S., Peng, J.M., Wang, R.S., Percussive-Rotary Drilling, Geological Publishing House, Beijing, (2010) 88-112.

[5] Wang, R.J., Jiang, R.Q., Han, J.Z., Liquid-Driven Percussive-Rotary Drilling, Geological Publishing House, Beijing, (1988) 97-104.

[6] Wang, D., Zhang, W., Zhang, X.X., Drilling Techniques for China Continental Scientific Drilling Engineering No.1 Well, Science Press, Beijing, (2007).

[7] Piao, C.Z., Yin, K., Jiang, R.Q., Wang, M.S., Experimental research on application of KSC-127 fluid efflux hammer in CSDP,. World Geol., 19(3) (2000) 295-298.

[8] Wang L., Wang W.G., Dou T.W., Xu L.H., Wang X.Y., Application of rotary percussion drilling technology in reverse thrust nappe structure formation, Oil Drill & Production Technol., 27(sup) (2005) 8-10.

[9] Wen, P., Chen, B., Lei, J.P., Yan, Y.C., Application of hydraulically impacting-rotary drilling technique in qingxi area of Yumen oil field, Nat. Gas Ind., 24(9) (2004) 64-67.

[10] Xiong, Q.S., Huang, Z.Q., Yin, K., Tian, H., Experimental research on a new type of hydro-efflux hammer in drilling deep and ultradeep wells, Nat. Gas. Ind., 28(12) (2008) 65-67.

[11] Shen, J.Z., He, Q., The application of model YSC-178 hydraulic jet hammer in rotary percussion drilling, China Petrol. Mach., 39(6) (2011) 52-54.

[12] Reisch, U., Meuer, R., CFD-simulation of the flow through a fluidic amplifier, Sensor Actuator A: Phys., 43(1-3) (1994) 330-334.

[13] Peng, J.M., Liu, H., Zhao, Z.Q., Bo, K., Wang, W., Erosion mechanism on outer wall of bottom plate of fluidic amplifier for YSC178A liquid jet hammer, J. Jilin Univ.-Earth Sci., 40(5), (2010) 1140-1144.

[14] Li, W.T., The Experiment and Research on the Working Life of the Liquid Jet Amplifier of the Hydraulic Hammer, M.E. Thesis of Jilin University, (2004) 20-50.

[15] ANSYS LS-DYNA User's Guide. Version 10.0, (2010).

[16] Chen, J.W., Research on Simulation and Experiment of Liquid Jet Hammer, Ph.D. Thesis of Jilin University, (2007) 39-113.

[17] Chen, J.W., Yin, K., Peng, J.M., Gu, L.Y., Zhou, B., Numerical simulation of the performance of the SC-89 jet impact system, Proceedings of the ASME dynamic systems and control conference-PTS A and B, (2010) 913-920.

[18] Li, G.L., Peng, J.M., Liu, H., Zhao, Z.Q., Prediction and verification of threshold flow velocity for jet nozzle of hammer hydro, J. Jilin Univ.-Earth Sci. 40(1) (2005) 159-163.

[19] Fluent User's Guide, Release 6.3.26, Ansys Inc. USA, (2006).

[20] Khelfaoui, R., Colin, S., Caen, R., Orieux, S., Baldas, L., Numerical and experimental analysis of monostable mini- and micro-oscillators, Heat Transfer Eng. 30 (1–2) (2009) 121–129.

[21] Wang, F.J., The Analysis of Computational Fluid Dynamics: CFD Software Principle and Application, Tsinghua University Press, Beijing, (2004).

[22] Specification for Threading and Gauging of Rotary Shouldered Thread Connections, API specification 7-2/ISO 10424-2, (2008) 67-79.

[23] He, T., Yang, J., ANSYS10.0/LS-DYNA Non-linear Finite Element Analysis, China Machine Press, Beijing, (2007).

[24] Ho, K.H., Newman, S.T., Rahimifard S., Allen R.D., State of the art in wire electrical discharge machining(WEDM), Int. J. Mach. Tool. Manu., 44 (2004) 1247-1259.

[25] Gatto, A., Luliano, L., Cutting mechanisms and surface features of WEDM metal matrix composite, J. Mater. Process Tech., 65 (1997) 209-214.